



**HAL**  
open science

# The effects of breathing mode oscillations on ion energy distribution function in Hall thrusters: Time-resolved RPA measurements

Quentin Delavière–Delion, F. Gaboriau, G. Fubiani, L. Garrigues

► **To cite this version:**

Quentin Delavière–Delion, F. Gaboriau, G. Fubiani, L. Garrigues. The effects of breathing mode oscillations on ion energy distribution function in Hall thrusters: Time-resolved RPA measurements. *Physics of Plasmas*, 2024, 31 (12), 10.1063/5.0235762 . hal-04856038

**HAL Id: hal-04856038**

**<https://hal.science/hal-04856038v1>**

Submitted on 26 Dec 2024

**HAL** is a multi-disciplinary open access archive for the deposit and dissemination of scientific research documents, whether they are published or not. The documents may come from teaching and research institutions in France or abroad, or from public or private research centers.

L'archive ouverte pluridisciplinaire **HAL**, est destinée au dépôt et à la diffusion de documents scientifiques de niveau recherche, publiés ou non, émanant des établissements d'enseignement et de recherche français ou étrangers, des laboratoires publics ou privés.



Distributed under a Creative Commons Attribution - NonCommercial 4.0 International License

**1 The effects of breathing mode oscillations on ion energy distribution  
2 function in Hall thrusters: time-resolved RPA measurements**

3 Quentin Delavière–Delion,<sup>1</sup> F. Gaboriau,<sup>1</sup> G. Fubiani,<sup>1</sup> and L. Garrigues<sup>1</sup>

4 *LAPLACE, Université Paul Sabatier, CNRS, INPT, 118 Route de Narbonne, 31062 Toulouse, France*

5 (\*Electronic mail: quentin.delaviere@laplace.univ-tlse.fr)

6 (Dated: 21 November 2024)

7 This paper presents a technique for reconstructing the temporal evolution of ion distribution functions (IDF) in a Hall  
8 thruster (HT) using ion currents measured with a retarding potential analyser (RPA). The method involves averaging  
9 discharge oscillations with temporal realignment based on the maxima of the discharge current. This technique was  
10 applied to ion currents from the experimental ID-Hall 2 thruster, successfully reconstructing the time-dependent ion  
11 distribution function (TIDF) in quasi-periodic plasma oscillation regimes. The results indicate that deformations in the  
12 integrated ion distribution function can be attributed to the IDF's temporal evolution over a characteristic time equal to  
13 the breathing mode oscillation period. This finding suggests the possibility of uncoordinated displacement of ionisation  
14 and acceleration zones within the discharge. In certain oscillation regimes, the oscillations in ion transit time also  
15 appear to have a minor effect on ion acceleration.

16 **I. INTRODUCTION**

17 Developed in the Soviet Union in the 1960s by Morozov's  
18 team<sup>1</sup>, Hall thrusters (HT) are electric propulsion systems  
19 used for spacecraft, including orbiting satellites and explo-  
20 ration probes. Ongoing advancements in Hall thruster tech-  
21 nology have led to their widespread adoption as the primary  
22 propulsion system in geostationary satellites<sup>2</sup>. Although they  
23 produce lower thrust than chemical thrusters, Hall thrusters  
24 offer a significantly higher specific impulse (ISP), which is  
25 proportional to the ion ejection velocity<sup>3,4</sup>.

26 **A. Hall thruster operation**

27 Despite their complex physics, Hall thrusters are simple to  
28 operate: a few hundred DC volts are applied between a cath-  
29 ode and an anode, and a radial magnetic field is established  
30 across the annular channel. This field traps electrons, increas-  
31 ing their residence time and enhancing gas ionisation. At the  
32 base of the channel and diffuses upstream toward the HT's  
33 exit plane, where it is ionised by collisions with high-energy  
34 electrons that have sufficient energy to cause ionisation to oc-  
35 cur. The resulting ions are accelerated by the electric field,  
36 generating thrust, and are neutralised by electrons from the  
37 cathode. The perpendicular electric and magnetic fields cre-  
38 ate a strong azimuthal electron drift current, sustained by the  
39 channel's annular shape. The interaction of electromagnetic  
40 fields, electron current, and plasma inhomogeneities gives rise  
41 to various instabilities over a wide frequency range (from a  
42 few hertz to several gigahertz) and wavelengths (from a few  
43 centimetres down to less than a millimetre).

44 **B. Axial instabilities in Hall thruster**

45 Low-pressure cross-field plasma sources, such as Hall  
46 thrusters, exhibit various instabilities that can lead to

47 oscillations<sup>5,6</sup> or turbulence<sup>7,8</sup>. Despite extensive experimen-  
48 tal and theoretical research, the properties and nature of some  
49 instabilities remain unclear. Understanding the dynamics of  
50 these instabilities is essential for addressing issues related to  
51 electron transport across magnetic barriers. In this paper, we  
52 consider two types of oscillations, each with distinct physical  
53 mechanisms, although they can coexist and both propagate  
54 axially.

55 The first type of instability in HT discharge, known as the  
56 breathing mode (BM), is characterised by long-period, high-  
57 amplitude oscillations on the discharge current, with frequen-  
58 cies ranging from a few kHz to tens of kHz. These oscillations  
59 have been widely observed in experiments<sup>9–16</sup> and resem-  
60 ble a predator-prey model<sup>17,18</sup>, with the frequency linked  
61 to gas flow and ionisation rates in the HT channel. The one-  
62 dimensional hybrid model by Garrigues & Boeuf<sup>19</sup> explains  
63 this behaviour as the result of efficient ionisation depleting  
64 neutral atoms faster than they can be replenished by the gas  
65 flow, causing the ionisation front to move towards the an-  
66 ode and reducing efficiency. This process leads to a cycli-  
67 cal pattern of virtual discharge extinction and renewed ion-  
68 sation. Although more advanced models exist<sup>20,21</sup>, predicting  
69 the characteristics of these BM oscillations remains challeng-  
70 ing due to interdependent mechanisms and potential interac-  
71 tions with other instabilities.

72 The second type of instability considered in this paper is  
73 ion transit time oscillations (ITTO), which occur at frequen-  
74 cies ranging from a few tens to a few hundreds of kHz and  
75 have been studied less extensively in experiments than BM os-  
76 cillations. These frequencies correspond to the inverse of the  
77 ion travel time through the acceleration zone. ITTO are multi-  
78 messenger oscillations that influence the discharge current,  
79 plasma potential, electric field, and ion distribution functions  
80 (IDFs). They can coexist with BM oscillations, though gener-  
81 ally with lower amplitudes. Similar oscillations have been  
82 observed in fluid<sup>22,23</sup>, hybrid<sup>17,24</sup>, and PIC-MMC models<sup>25</sup>.  
83 ITTO are characterised by oscillations in the potential distri-

1 bution within the thruster channel, which can propagate into 54  
 2 the plume. These potential oscillations affect ion acceleration: 55  
 3 some ions gain additional energy through resonant accelera- 56  
 4 tion with the electric field waves, while others are slowed 57  
 5 down. This results in distorted ion velocity distribution func- 58  
 6 tions, perturbed ion currents (and consequently also the dis- 59  
 7 charge current  $I_d = I_{e,i} + I_{e,c}$ ) and altered ion density profiles, 60  
 8 which in turn impact the potential distribution.

### 9 C. Time-resolved IDF reconstruction techniques 64

10 In conventional use, the RPA measures the average ion 66  
 11 distribution function (IDF). To achieve this, a voltage ramp is 67  
 12 applied to the RPA discriminator grid at a frequency on the 68  
 13 order of Hertz, which is significantly lower than the plasma 69  
 14 oscillation frequencies. This slow ramping averages out any 70  
 15 potential effects from these oscillations in the collected signal. 71

16 Since the time-averaging principle of the conventional 72  
 17 RPA method does not allow the study of possible changes in 73  
 18 the IDF over characteristic instability times, it is inadequate 74  
 19 for the study of low-frequency oscillations in the HT dis- 75  
 20 charge, which occur at frequencies ranging from a few kHz to 76  
 21 MHz. Despite their importance for understanding the mech- 77  
 22 anisms driving instabilities and their impact on thruster per- 78  
 23 formance, there are relatively few references in the literature 79  
 24 focusing on time-resolved IDF (TIDF) measurements using 80  
 25 an RPA.

26 Only a handful of studies have used an RPA to track 83  
 27 ions during BM oscillations<sup>13,26–30</sup>, though interest in this 84  
 28 area has resurged in recent years. Such advances have been 85  
 29 made possible by innovative techniques, enhanced computa- 86  
 30 tional capabilities, and improved plasma discharge control. 87  
 31 However, some challenges remain, such as discharge irreg- 88  
 32 ularities, which necessitate the development of noise-resistant 89  
 33 techniques.

34 Time-resolved measurements using LIF (laser-induced 90  
 35 fluorescence)<sup>31,32</sup> have shown results comparable to those ob- 91  
 36 tained with RPA-collected signals. 92

37 While all RPA-based reconstruction techniques rely on 94  
 38 a similar data acquisition protocol, as described in subsec- 95  
 39 tion III A, various signal processing methods are available 96  
 40 for reconstructing TIDFs. These include the empirical trans- 97  
 41 fer function<sup>27,28,33</sup>, time realignment<sup>13,14</sup>, shadow manifold 98  
 42 interpolation<sup>29,30,33</sup>, and their variants, with or without dis- 99  
 43 charge forcing<sup>34</sup>. Each method has its own advantages and 100  
 44 limitations. 101

45 **Empirical Transfer Function (ETF):** Using a reference sig- 102  
 46 nal ( $I_d$ ), the empirical transfer function reconstruction method<sup>103</sup>  
 47 allows for the alignment of signals onto a common basis<sup>104</sup>  
 48 through normalisation and transformations in Fourier space.

49 While this method is advantageous for its simplicity of im- 105  
 50 plementation, a major drawback lies in the transfer function's 106  
 51 low resilience to noise. To improve the signal-to-noise ratio,<sup>107</sup>  
 52 the signal frequency and sampling depth can be increased dur- 108  
 53 ing data acquisition. However, this results in larger datasets,<sup>109</sup>

making them more challenging to handle. For instance, in 110  
 the study by<sup>27</sup>, the authors report that each time series re- 111  
 quires several million, if not billions, of data points. Further 112  
 noise reduction in the transfer function can be achieved by 113  
 averaging the FFTs calculated over sliding time windows<sup>28</sup> 114  
 when computing the complex series. Despite these enhance- 115  
 ments, tests conducted with a perfectly known, controllable, 116  
 and adjustable ion source<sup>33</sup>, revealed that the Fourier space 117  
 transfer function method fails to accurately reconstruct noisy 118  
 sinusoidal signals. This limitation arises because the trans- 119  
 fer function reconstruction method remains highly sensitive 120  
 to experimental noise<sup>35</sup>.

**Shadow Manifold Interpolation (SMI):** The SMI method 121  
 is an innovative nonlinear mapping technique derived from 122  
 the field of nonlinear dynamic system analysis. Studies con- 123  
 ducted in<sup>33,35</sup> demonstrate the superiority of SMI reconstruc- 124  
 tion for short, noisy, and weakly aperiodic signals compared 125  
 to the ETF method, which relies on FFT. Furthermore, achiev- 126  
 ing similar results with SMI requires 15 to 100 times fewer 127  
 data points than ETF-based approaches<sup>28</sup>. This significantly 128  
 reduces the database size, allowing for the exploration of a 129  
 broader range of filter voltages, though SMI remains compu- 130  
 tationally demanding. While SMI is more complex to imple- 131  
 ment than transfer function methods, this alternative approach 132  
 to temporal reconstruction appears promising<sup>29,30,33</sup>. How- 133  
 ever, it currently shows effective results only when the dis- 134  
 charge signal is sufficiently periodic and lacks frequent inter- 135  
 mittent oscillations across various frequencies. Indeed, a rapid 136  
 decrease in signal-to-noise ratio is observed as the frequency 137  
 of the oscillations increases<sup>33</sup>.

**Discharge Modulation:** To address discharge irregularities, 138  
 particularly variations in the central BM frequency, an exter- 139  
 nal forcing can be applied to modulate the discharge voltage. 140  
 This external modulation aligns the "natural" oscillations, sta- 141  
 bilizing the discharge dynamics over time and making them 142  
 temporally coherent<sup>34</sup>. By reducing discharge variability, this 143  
 technique enhances the signal-to-noise ratio, facilitating the 144  
 study of temporal evolution of plasma parameters such as dis- 145  
 tribution functions at different oscillation phases. Since this 146  
 technique is hardware-based, it can be used alongside other 147  
 data processing methods. However, it assumes that the nat- 148  
 ural plasma dynamics remain largely unaffected, which may 149  
 not always hold true. Moreover, implementing such a system 150  
 is complex and resource-intensive. Consequently, we have 151  
 opted not to use this technique in our study.

**Temporal alignment:** Among all the previous techniques, the 152  
 time realignment method is the easiest to conceptualize. The 153  
 general idea is to shift the oscillation patterns in the different 154  
 data series to best align them with a reference signal<sup>14</sup>. The 155  
 corresponding ion currents are then extracted for each filtering 156  
 voltage, after which the TIDF is calculated.

All these methods require reproducible and periodic 157  
 plasma oscillations, as any instability in the central frequen- 158  
 cies could significantly compromise the quality of the recon- 159  
 structed IDF. Here, we opted to use a time alignment tech- 160  
 nique based on a reference signal that must be periodic, rep-

1 representative of the discharge, and unaffected by variations in 49  
2 the RPA settings. In this paper, the discharge current  $I_d$  was 50  
3 chosen as this indicator, although the capacitive signal  $S_{\text{capa}}$  51  
4 could also serve this purpose. 52

5 The aim of this paper is to investigate the effect of axial 54  
6 oscillations on both time-averaged and temporal ion velocity 55  
7 distribution functions. Following an introduction to our ex- 56  
8 perimental setup and the HT used (section II) we will briefly 57  
9 discuss and present the different techniques for reconstructing 58  
10 time-resolved ion distribution functions (TIDF) in the section  
11 IC and we will outline the principle of conventional RPA mea-  
12 surements (subsection II B 2).

13 We have chosen to use the time realignment technique 59  
14 based on detecting the peak of the discharge current to align 60  
15 the average oscillations. Section III details our method 61  
16 for temporally resolving IDFs at the frequencies of BM 62  
17 and ITTO. We then apply this method to reconstruct time- 63  
18 dependent IDFs in stable oscillation regimes, discussing possi- 64  
19 ble ion energy variations in relation to changes in discharge 65  
20 current and capacitive signals (section IV). Finally, we con- 66  
21 clude by highlighting the appropriate applications of this 67  
22 method.

## 23 II. EXPERIMENTAL SET-UP

### 24 A. The ID-Hall 2 Thruster and Vacuum Testing Facility

25 The results presented in this paper were obtained using the 74  
26 ID-Hall 2 experimental thruster, equipped with a MIREA-type 75  
27 emitting cathode<sup>36</sup>, with a constant thermal power dissipation 76  
28 of 240 W. This section briefly reviews the main discharge pa- 77  
29 rameters. Designed at the LAPLACE laboratory, the thruster 78  
30 operates in single-stage mode without an RF coil, similar to 79  
31 a standard cylindrical HT. The cathode gas flow rate is main- 80  
32 tained at 0.25 mg/s of xenon, while thruster gas flow rates 81  
33 were tested between 0.6 and 0.9 mg/s. The pumping system 82  
34 maintains a pressure of approximately  $10^{-4}$  mbar ( $10^{-2}$  Pa). 83  
35 To better represent spaceflight conditions, the thruster's elec- 84  
36 trical system is kept floating relative to the ground, with the 85  
37 cathode common as the reference potential (indicated by the 86  
38 blue wires in the figure 1). For more detailed information on 87  
39 the ID-Hall 2 thruster, please refer to<sup>37</sup>. 88

### 40 B. Diagnostics

#### 41 1. Measurement of Time-Varying Properties 90

42 The following measurements were performed directly on 91  
43 a digital oscilloscope with a  $1\text{ M}\Omega$  input impedance: 92

- 44 • The discharge current  $I_d$  is measured via an  $NT-5$  93  
45 magneto-resistive sensor placed between the anode and 94  
46 the discharge voltage generator (green circle in figure  
47 1), which outputs a voltage proportional to the dis-  
48 charge current.

- The potential difference  $V_{\text{cg}}$  between the cathode and  
ground is measured at the green point in figure 1.
- The voltage at the electrical poles of a capacitive an-  
tenna  $S_{\text{capa}}$ , positioned outside the chamber against the  
quartz side window of the vessel, which detects all elec-  
tromagnetic disturbances induced by the plasma. The  
probe's position was varied along the glass window,  
with no significant changes in signal shape observed at  
frequencies below a tenth of MHz.

#### 2. IDF averaged over time

A four-grid Retarding Potential Analyser (RPA) was used  
to measure the mean ion distribution functions in the thruster  
plume; further design details can be found in the referenced  
PhD thesis<sup>38</sup>. The RPA is mounted on an arm that positions  
the screening grid 41 cm from the thruster exit plane, placing  
the RPA collector approximately 44 cm from the thruster exit  
plane.

The RPA is used to filter ions based on their kinetic en-  
ergy, allowing only selected ions to be detected. Using four  
independently polarised grids (figure 2), the RPA works as fol-  
lows: Grid G1, the shielding grid, isolates the plasma from the  
instrument's electric field and is left floating. (with  $U_{G1} = V_f$ ).  
Grid G2, the electron repulsion grid, is negatively polarized  
at  $U_{G2} = -35$  V, to repel electrons from the plasma, allow-  
ing only ions to pass. Grid G3, the ion discriminator/filter  
grid, creates a potential barrier  $\phi_{\text{RPA}}$  that only ions with suf-  
ficient energy can cross, contributing to the collected current.  
Grid G4, an additional electron repulsion grid, is polarised at  
 $U_{G4} = -40$  V to send back secondary electrons emitted by the  
collector as a result of ion bombardment.

The resulting collector current  $I_{\text{RPA}}$ , generated by ions  
impacting the collector C, is proportional to the ion cur-  
rent density  $J_{\text{RPA}}$  entering the RPA with a kinetic energy  $E_k$   
greater than the minimum required to cross the potential bar-  
rier ( $J_{\text{RPA}}(\phi_{\text{RPA}}) = J_{\text{RPA}}(E_c > q_i e \phi_{\text{RPA}}) = J_{\text{RPA}}(v_{\text{min}})$ ), with  $e$   
the elementary charge,  $q_i$  the charge number of the ions and  
 $v_{\text{min}}$  the minimum velocity required to cross the potential bar-  
rier  $\phi_{\text{RPA}}$ :  $v_{\text{min}} = \sqrt{\frac{2q_i e \phi_{\text{RPA}}}{m_i}}$ , while  $m_i$  is the mass of the ion),  
and can be measured using an oscilloscope. The relationship  
between the current collected by the RPA and the ion current  
density can be written as:

$$I_{\text{RPA}} = J_{\text{RPA}}(v_{\text{min}}) S_{\text{RPA}} \tau_{\text{tr}} \quad (1)$$

Where  $S_{\text{RPA}}$  is the surface area of the RPA collection zone  
and  $\tau_{\text{tr}}$  is its transparency. These two parameters are unknown  
to us. And:

$$J_{\text{RPA}}(v_{\text{min}}) = q_i e n_i \int_{v_{\text{min}}}^{+\infty} v f(v) dv \quad (2)$$

This is the author's peer reviewed, accepted manuscript. However, the online version of record will be different from this version once it has been copyedited and typeset.

PLEASE CITE THIS ARTICLE AS DOI: 10.1063/1.50235762

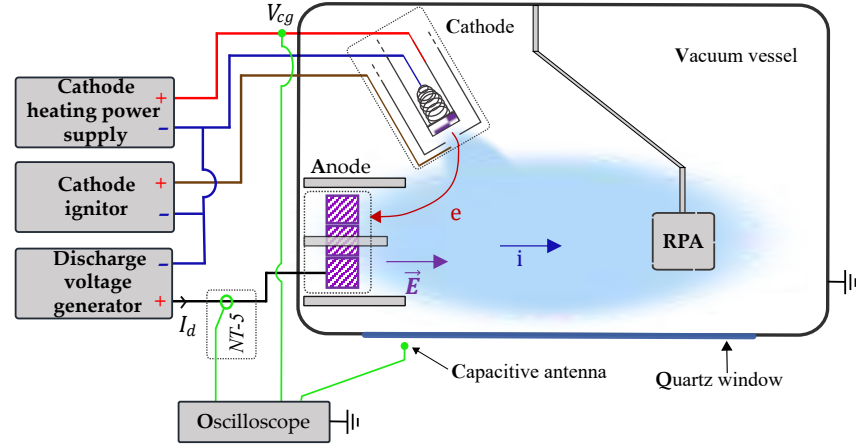


FIG. 1. Thruster electrical circuit schematic diagram.

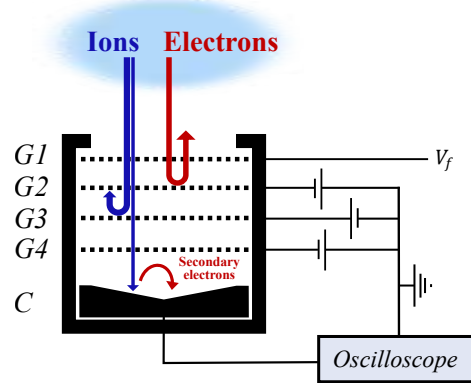


FIG. 2. Sketch of the retarding potential analyser and its connections.

1 In the previous equation, the ion velocity distribution  
2 function (IVDF) is denoted by  $f(v)$ , where  $v$  is the ion ve-  
3 locity, and  $n_i$  is the ions density. By combining the equation  
4 (1) and (2), we obtain :

$$5 \quad f(v) = -\frac{1}{S_{RPA} \tau_{tr}} \frac{m_i}{n_i q_i^2 e^2} \frac{dI_{RPA}(\phi_{RPA})}{d\phi_{RPA}} \quad (3)$$

6 And so:

$$7 \quad f(v) \propto -\frac{dI_{RPA}(\phi_{RPA})}{d\phi_{RPA}} \quad (4)$$

8 It is important to clarify that the IVDF is directly propor-  
9 tional to the derivative of the collected current with respect  
10 to the potential applied to the RPA. In this paper, we refer to  
11 an ion velocity distribution function (IVDF, or IDF hereafter),  
12 not an ion energy distribution function (IEDF). The confusion  
13 often arises from the conventional use of energy units (eV) to  
14 express velocities. The IEDF  $g(E)$  is given by the following  
15 formula, where energy is represented by  $E$ :

$$16 \quad g(E) = f(v) \frac{1}{m_i v} \quad (5)$$

17 An additional correction is required to account for the po-  
18 tential difference between the thruster's floating electrical sys-  
19 tem and the ground-referenced RPA. This is done by subtract-  
20 ing  $q_i V_{cg}$  from the measured ion energy, where  $q_i = 1$  (con-  
21 sidering only singly charged ions).

22 In practice, a voltage ramp is applied to the discrimina-  
23 tor grid using a voltage generator controlled by a function  
24 generator, which provides a triangular reference signal with  
25 a selected frequency and amplitude. The voltage ramp limits  
26 are chosen to encompass the ion current  $I_{RPA}$  variation range  
27 of the IDF for each operating condition. The frequency of  
28 the voltage ramp is set at 0.5 Hz, which is much below the  
29 plasma oscillation frequencies, to average out any potential  
30 effects from these oscillations in the collected signal. The os-  
31 cilloscope measures both the current from the RPA collector

1 and the voltage applied to the filter grid. To reduce noise, each  
2 measurement series is averaged over 16 cycles on the oscillo-  
3 scope. Before calculating the IDF, the measured signals are  
4 filtered using the standard Savitzky-Golay<sup>39,40</sup> algorithm to  
5 minimise noise that could be amplified by the derivative calcu-  
6 lation in equation (4). The resulting IDFs are then further  
7 processed using the Savitzky-Golay algorithm for final filter-  
8 ing.

### 9 III. TIME-RESOLVED IDF RECONSTRUCTION

10 The time-averaging principle of the previous conventional  
11 RPA method (subsection II B 1) does not permit the investiga-  
12 tion of potential changes in the IDF during the characteris-  
13 tic instability times. The target low-frequency oscillations in  
14 the HT discharge have frequencies ranging from a few kHz  
15 to MHz, whereas the ion population measurements are con-  
16 ducted at a much lower frequency of 0.5 Hz.

#### 17 A. Data acquisition

18 To capture the IDF dynamics during multiple oscillations,  
19 one could consider increasing the voltage ramp frequency.  
20 However, generating a complete I/V trace at the Nyquist fre-  
21 quency of the oscillation is challenging due to the limited  
22 availability of variable voltage generators capable of sweep-  
23 ing 300 V at several hundred kHz, as well as capacitive effects  
24 within the instrument. A simpler alternative approach is to set  
25 a constant filter potential on the filter grid,  $\phi_{RPA,m}$ , and record  
26 the time series of the collected current,  $I_{RPA}(t, \phi_{RPA,m})$ , for this  
27 filtering voltage. The filter voltage is then changed to  $\phi_{RPA,n}$ ,  
28 and the acquisition of  $I_{RPA}(t, \phi_{RPA,n})$  is repeated until the en-  
29 tire area of interest is scanned, as determined by examining  
30 the average IDF.

31 During data acquisition, the potential associated with the  
32 discharge current, the capacitive potential of an antenna out-  
33 side the vacuum vessel, the current collected by the RPA, and  
34 the cathode potential relative to ground are simultaneously  
35 recorded on a digital oscilloscope. However, direct current  
36 measurement requires conversion to voltage using Ohm's law,  
37 where the current passes through a measuring resistor with a  
38 known resistance value ( $R_m = 1 \text{ M}\Omega$ ) and considering capac-  
39 itive effects modelled by a capacitance ( $C_o = 11 \text{ pF}$ ), as pro-  
40 vided by the manufacturer. The cut-off frequency at  $-3 \text{ dB}$  is  
41 given by  $f_{c,oscilloscope} = \frac{1}{2\pi R_m C_o} \approx 14 \text{ kHz}$ .

42 To avoid low-pass filtering effects of the oscilloscope, a  
43 *Hamamatsu C12419* current-to-voltage converter, combined  
44 with a broadband amplifier, was used to measure the ion cur-  
45 rents. To minimise measurement noise, it is standard practice  
46 to average the signals directly on the oscilloscope, regardless  
47 of the data processing technique applied. Thus, recordings  
48 were obtained by averaging the signals 16 times.

#### B. Data Verification

Before aligning the data, it is essential to check the  
validity of the measurements. One way for doing this is to  
compare the currents collected using the traditional, integrated  
RPA method with those obtained through a time-averaging ap-  
proach at a set of fixed filter voltages. This process involves  
averaging each time series  $I_{RPA}(t, \phi_{RPA})$  to calculate the time-  
averaged current  $\overline{I_{RPA}}(\phi_{RPA}) = \langle I_{RPA}(\phi_{RPA}, t) \rangle_t$ , which is then  
compared with the integrated current  $I_{RPA}(\phi_{RPA})$  obtained via  
the conventional method.

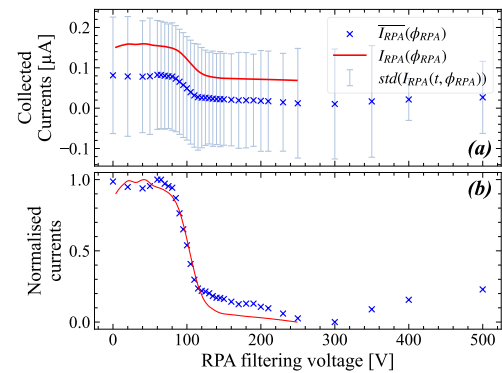


FIG. 3. Comparison of the ions collected currents using the RPA with a voltage ramp (red solid curve) and by averaging the ions time series for each filter voltage (blue crosses). (a): Direct current comparison, the vertical bars indicates the standard deviation of the ion current oscillations over the time series. (b) Current comparison after normalisation by an affine function. ID-Hall 2 with 0.9 mg/s Xenon at  $U_d = 120 \text{ V}$ .

The top graphs in figure 3 illustrates this comparison, revealing that while trends appear similar, the integrated current values (red solid curve), obtained with conventional use of RPA, are consistently higher than those of the time-averaged current (blue crosses). This discrepancy can be attributed to the oscilloscope's signal averaging function, which, while effective at reducing noise, also dampens oscillations that are not perfectly periodic. In order to compare the signals more easily, we have plotted in figure 3 (b) the average ion currents normalised by an affine function depending on the extreme values of the ion current (blue crosses):  $I_{RPA,normalised} = \frac{I_{RPA} - \min(I_{RPA})}{\max(I_{RPA}) - \min(I_{RPA})}$ . It shows that the fit is much better, reflecting similar ion behaviour in the discharge. In figure 3 (a), the standard deviation of the oscillations is given for each ion filter voltage. The values are sometimes greater than the mean current itself. This shows that the signals are noisy and that prior filtering of the data is necessary before they can be used. The Savitzky-Golay algorithm was applied for smoothing when analyzing the mean values shown in the figures throughout this section.

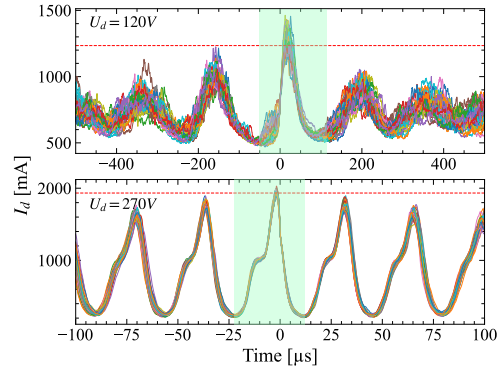


FIG. 4. Discharge currents  $I_d$  averaged over 16 cycles by the oscilloscope for a gas flow rate of 0.9 mg/s of xenon for  $U_d = 120$  V (top) and  $U_d = 270$  V (bottom). Each coloured curve corresponds to a different RPA filter voltage.

The discrepancy between the ions collected currents is largely due to the oscilloscope's signal averaging function. While averaging effectively reduces noise, it also dampens oscillations that are not perfectly periodic. As a result, the mean signal value is estimated more accurately, but the amplitude diminishes more rapidly when computed across numerous samples with varying oscillation frequencies, as shown in figure 4.

For relatively stable and periodic discharges, changes in the breathing mode (BM) frequency reduce the total amplitude by about one-third over three periods. However, in more irregular discharges, this instability leads to an amplitude reduction of nearly half over the same period. Therefore, to achieve reliable results, it is essential to remain close to the initial trigger time, ideally within the green transparency region. This phenomenon is an artifact resulting from the combination of averaging, irregular oscillation frequencies, and the oscilloscope's trigger threshold effects, explaining why oscillations centered around time zero tend to exhibit the closest resemblance.

The ion distribution functions (IDFs) associated with the currents  $I_{RPA}(\phi_{RPA})$  and  $\overline{I_{RPA}}(\phi_{RPA})$  (figure 3) can be calculated using (4), with the corresponding IDF graphs shown in figure 5. While the two IDFs are very similar, slight differences between them are observed. These discrepancies can be attributed to several factors:

- **Sampling Differences:** The sampling steps differ slightly between integrated and time-based measurements, which can cause a minor energy offset in the derivative calculations.
- **Deviation of the thruster's behaviour over time:** After many hours of operation, the thruster exhibits slight deviations. This is likely the most significant factor contributing to the observed differences in the two distribu-

tions.

Despite these minor discrepancies, they are minimal enough to validate the robustness of this procedure.

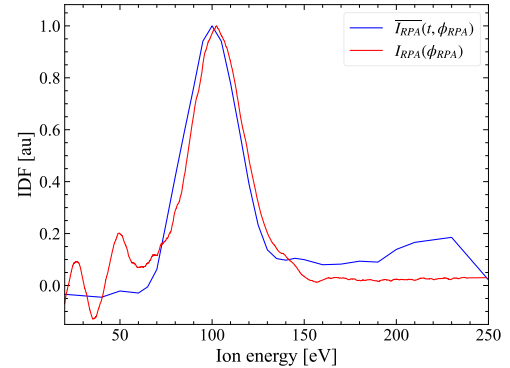


FIG. 5. Comparison of IDF obtained by direct derivation of RPA current as a function of retarding potential (red curve) and from time series averaging (blue curve) for the same conditions than in figure 3.

## C. Data Processing

### 1. Temporal alignment of the data

To minimize noise in the signals, the first step involves filtering the time-series data. To achieve optimal noise reduction, the data were oversampled during acquisition, allowing for more effective filtering. Fourier space filtering is chosen for this purpose, removing all oscillations with frequencies above the set cut-off frequency of  $f_c = 1$  MHz.

The following steps aim to synchronize the different time series to reconstruct the currents relative to the RPA filter voltage and a unified time frame. Since the only variable between time series is the RPA barrier potential,  $I_d$  is assumed to be fully reproducible and is thus used as the reference signal to synchronize the time series (using the capacitive signal as an alternative reference yields identical results).

The reconstruction protocol for time series begins by pinpointing a reference time in each series' discharge current, specifically by identifying the peak current within the BM oscillation closest to the measurement start. To achieve this, a local maximum search algorithm identifies prominent peaks based on relative amplitude and prominence, isolating the most significant oscillation peak. Once this peak's position,  $t_{\max(I_d)}$ , is determined, the time series is constrained to the interval  $[t_{\max(I_d)} - T_{BM}/2, t_{\max(I_d)} + T_{BM}/2]$ , where  $T_{BM}$  represents the BM oscillation period. It is determined by inverting the frequency that corresponds to the peak in the spectral power density of the discharge current time series. This

This is the author's peer reviewed, accepted manuscript. However, the online version of record will be different from this version once it has been copyedited and typeset.

PLEASE CITE THIS ARTICLE AS DOI: 10.1063/1.50235762

1 frequency is identified through the calculation of the FFT of  $I_d(t)$ .

2  
3 This procedure is repeated across all series to achieve temporal alignment. A quick verification of alignment can be performed by superimposing the discharge currents, as illustrated in figure 6. Although alignment improves, some discrepancy remains due to the discharge's non-periodic oscillations, suggesting that this method may not be ideal for conditions with high irregularity in discharge behavior.

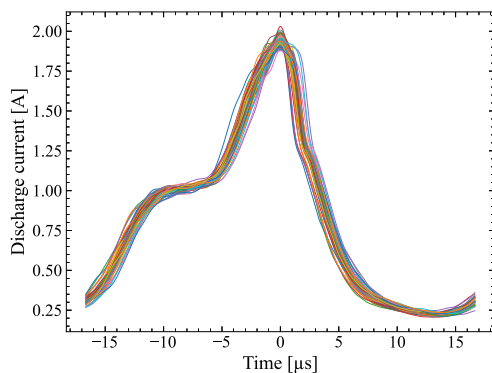


FIG. 6. Superimposed discharge currents for a fixed discharge voltage of 270 V. Each coloured curve corresponds to a different RPA filter voltage.

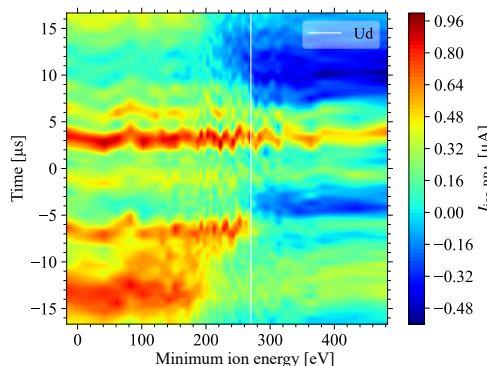


FIG. 7. 2D map of ion current collected by the RPA as a function of the potential applied to the discriminator grid corrected from the cathode to ground voltage for a fixed discharge voltage of 270 V.

10 For improved clarity, figure 7 presents a 2D map of the ion  
11 current collected by the RPA as a function of both a common  
12 reference time and the energy needed for ions to overcome  
13 the potential barrier. The reference time origin is defined as  
14 the moment when occur the maximum peak  $I_d$  within the BM

oscillation cycle. To obtain this map, an extra processing step is performed: the voltage difference between the cathode and ground is subtracted from the RPA filter voltage, ensuring that the map reflects true ion energy.

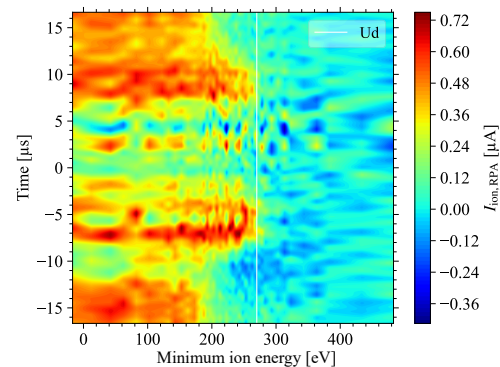


FIG. 8. Same map of the ion current collected by the RPA than the figure 7, but corrected for capacitive effects.

19 In the map, prominent continuous bands are visible across  
20 various energy levels at time points  $-1$ ,  $4$ , and  $6$   $\mu$ s. Given  
21 the discharge voltage of  $U_d = 270$  V, it is highly improbable that  
22 ions reach energies beyond  $450$  eV through normal acceleration  
23 processes. This pattern suggests that capacitive effects within the  
24 RPA and along its acquisition line, likely triggered by fluctuations  
25 in the plasma potential in their vicinity, are influencing the  
26 measurements. This hypothesis aligns with findings from previous  
27 studies, such as those in<sup>27</sup>. Assuming that these capacitive effects  
28 are independent of the sampled ion energy and remain periodic in  
29 time for fixed discharge conditions, the average of the currents  
30 measured above one hundred volts above the discharge voltage is  
31 subtracted from the ion currents at each probed time. This involves  
32 subtracting ion currents collected with RPA potential barrier settings  
33 between  $370$  and  $500$  V for a discharge voltage of  $270$  V, resulting  
34 in the new current map shown in figure 8.

## 36 2. Calculation of the TIDF

To obtain the IDF as a function of time, the collected ion current is differentiated along the energy axis according to equation (4). Before performing this differentiation, the currents are filtered along the energy axis to reduce strong fluctuations caused by irregularities in the discharge over time using Savitzky-Golay's algorithm. The resulting graph,  $IDF(t, E_k)$ , shown in figure 9, represents the evolution of the ion energy distribution during a BM period, illustrating how the distribution changes dynamically throughout the oscillation.



This is the author's peer reviewed, accepted manuscript. However, the online version of record will be different from this version once it has been copyedited and typeset.

PLEASE CITE THIS ARTICLE AS DOI: 10.1063/5.0235762

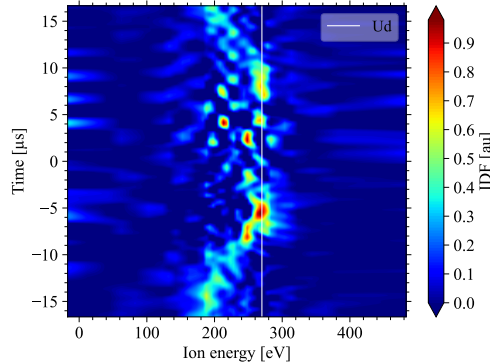


FIG. 9.  $IDF(t, E_k)$  2D map for  $U_d = 270$  V at the RPA location in the RPA time frame.

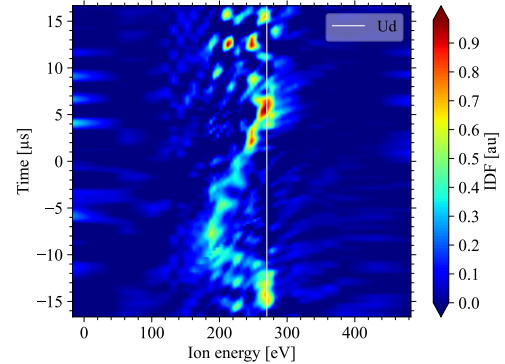


FIG. 10.  $IDF(t, E_k)$  2D map for  $U_d = 270$  V at the thruster exit plane level.

1 **3. Correction from flight time**

2 To facilitate comparison with other measured quantities, 26  
 3 the IDFs were corrected for distortions caused by the flight 27  
 4 time of ions as they travel from the extraction zone to the RPA. 28  
 5 Assuming that the ions are no longer accelerated beyond the 29  
 6 thruster exit plane, the IDFs were reconstructed at the thruster  
 7 exit plane using equations (6) and (7). For each current def- 30  
 8 ined by collection time and minimum energy, the IDF time 31  
 9 axis alignment was calculated considering the following fac- 32  
 10 tors: 33

- 11 •  $t_{RPA}$  : signal pickup time 34
- 12 •  $t_{exit\ plane}$  : ion emission time 35
- 13 •  $\Delta t_{flight\ time}$  : ion time of flight 36
- 14 •  $d_{RPA-exit\ plane}$  : distance between thruster exit plane and 37  
 15 RPA manifold 38

16 
$$t_{exit\ plane} = t_{RPA} - \Delta t_{flight\ time} \quad (6)$$

17 
$$\Delta t_{flight\ time} = d_{RPA-exit\ plane} \cdot \sqrt{\frac{m_{Xe}}{2e(\Phi_{RPA} - V_{cg})}} \quad (7)$$

18 This alignment implies that each energy level must be 46  
 19 shifted by a time equivalent to the time it takes for the ions 47  
 20 to reach the RPA, with more energetic ions having shorter 48  
 21 travel times. The resulting transformation is shown in figure 10. 49

22 **4. Determination of uncertainties**

23 The uncertainty in the ion energy profile arises from sev- 54  
 24 eral sources: 55

- The uncertainty in the voltage supplied by the generator and applied to the filter grid is 0.5 V. This could introduce a slight shift in the measured ion energies, which would manifest as a small uncertainty in the absolute energy values of the ions.
- Fluctuations in the cathode coupling potential relative to ground have maximum amplitudes of 3 V, but the RPA measurement step is at least 5 V in the ion current variation regions. These fluctuations cannot be corrected and are masked by voltage sampling resolution.
- Potential drop loss in the electrostatic sheath at the RPA input. Assuming that plasma potential fluctuations are transmitted with the same amplitude and phase at the sheath output, floating potential fluctuations equal plasma potential fluctuations, with only their average values differing. This hypothesis is verified for fluctuations below 1 MHz<sup>41</sup>.

The total uncertainty in ion energy is estimated to be about 5 eV. This uncertainty only affects the absolute energy values, and not the temporal position of the energy distribution in the following TIDF.

The uncertainty in the time adjustment is determined by considering the uncertainty in the distance between the RPA collector and the ion extraction zone (in this work, we have considered  $\pm 3$  cm), as well as the velocity of the ions. This uncertainty depends on the energy of the ions and is shown in the graph in figure 11. It is obtained by calculating the time of flight taking into account the distance uncertainty for an ion with a kinetic energy between 1 and 500 eV. In the IDF variation range between 200 and 300 V, the uncertainty is ranging between 2 and 1.5  $\mu$ s, respectively.

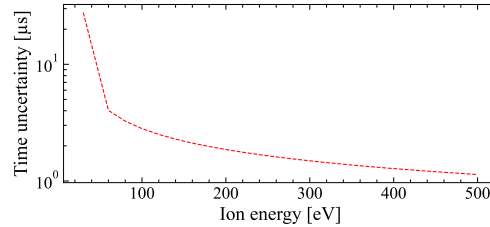


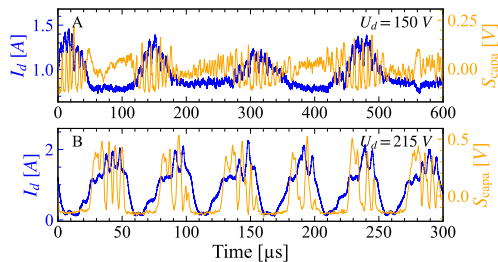
FIG. 11. Overall time shift uncertainty.

## IV. RESULTS & DISCUSSION

### A. Oscillation regimes in ID-Hall 2 plasma

Several oscillation regimes were identified in a previous study<sup>37</sup>, which provides a detailed analysis of the discharge current behavior across different operating conditions. These regimes are characterized by distinct patterns of BM oscillations and ITTO, which play a significant role in shaping the plasma dynamics within the thruster :

- Regime A: This regime corresponds to low-frequency BM oscillations occurring within a discharge voltage range of  $U_d \in [105 - 175]$  V. In this regime, the discharge current behavior is illustrated in the top graph in figure 12.
- Regime B: For  $U_d \in [175 - 335]$  V, the BM oscillations become higher in frequency and amplitude.  $I_d$  is characterized by larger oscillations, as shown in the bottom graph in figure 12.
- Regime C: For  $U_d \in [335 - 408]$  V, the BM oscillations become unstable, with a significant increase in the electronic current transmitted to the anode.

FIG. 12. A time series examples in A and B regimes, with the  $I_d$  shown in blue and the capacitive signal ( $S_{\text{capa}}$ ) in orange.

Throughout all the regimes, BM oscillations are observed, albeit transiently in some cases, accompanied by fast oscillations in the tens to hundreds of kHz range during the peak of the discharge current. These fast oscillations correspond to signal peaks detected by the external capacitive antenna (the

orange curves in figure 12), which suggests a correlation between ion current variations and electric field reorganization in the plasma. This finding supports the hypothesis that these fast oscillations are ITTOs, likely related to the time it takes for ions to travel across the plasma.

In Regime B, in particular, the overlap of high-frequency oscillations with the BM harmonic frequencies, combined with the doubling of discharge current oscillation amplitudes, points to a possible resonant interaction between these two types of oscillations. For a more detailed exploration of the oscillation regimes and their associated behaviors, the comprehensive study in reference<sup>37</sup> provides further insights.

### B. Mean ion distribution functions

Using an RPA, IDFs were measured for different discharge voltages, revealing distinct patterns that correlate with the previously identified plasma oscillation regimes. The data, shown in figure 13, illustrates two major groups of IDF shapes: a relatively symmetric distribution at low and high voltages (regimes A and C) and an asymmetrical distribution like the sum of two shifted Gaussians in regime B. In this regime, as the discharge voltage increases, a second peak gradually develops on the high energy side, while the initial probability maximum shifts towards the lowest energies. The second peak becomes more prominent and the low energy peak gradually disappears, marking the transition to regime C. This suggests that plasma oscillations significantly influence the overall ion dynamics.

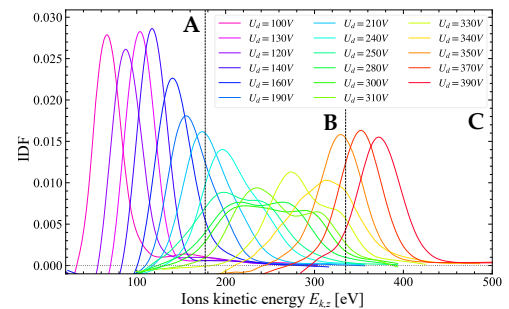


FIG. 13. IDF given for some discharge voltages with a xenon flow rate of 0.9 mg/s. The black dashed lines mark the boundary discharge voltages between the different plasma oscillation regimes: A, B and C.

The energy positions of the main IDF peaks are approximately shifted with respect to the applied plasma discharge voltage:

- between 15 and 30 eV in the low-amplitude BM oscillation zone (regime A);
- about 60 eV (low energy peak);

- 1 • about 0 eV (high energy peak) in the high-amplitude 52  
 2 BM oscillation range (regime B). 53

3 Whatever the oscillation regime, we observe that a signif- 54  
 4 icant proportion of the ions would be super-energetic, acquir- 55  
 5 ing more kinetic energy than the available potential energy 56  
 6 imposed by the discharge voltage. 57

7 While symmetrical Gaussian-shaped distributions are 58  
 8 common and relatively easy to explain, asymmetrical distribu- 59  
 9 tions are not. There are three hypotheses to explain the asym- 60  
 10 metric distributions observed in RPA measurements, which 61  
 11 result from both temporal and spatial integration: 62

12 • Ions are created in different regions and experience dif- 63  
 13 ferent acceleration potentials. Plume measurements using 64  
 14 a series of three Langmuir probes showed no varia- 65  
 15 tions in ion current shape or flight time within the mea- 66  
 16 surement domain, limiting the applicability of this hypo- 67  
 17 thesis to areas inaccessible to the probes, such as the 68  
 18 end of the thruster channel or the first few centimetres 69  
 19 of the plume. 70

20 • Ions are accelerated by the same potential drop, but 71  
 21 from radially distant locations, which would affect the 72  
 22 transfer function of the RPA<sup>42</sup>. However, a hemispheri- 73  
 23 cal scan using the RPA revealed no change in the shape 74  
 24 of the IDF over the first thirty degrees, only a variation 75  
 25 in the intensity of the collected ion current. This obser- 76  
 26 vation rejects the hypothesis. 77

27 • Ions of different energies are produced at different 78  
 28 times, corresponding to different phases in the progres- 79  
 29 sion of the oscillations. This hypothesis aligns with the 80  
 30 findings of a recent 2D PIC-MCC simulation study<sup>25</sup> 81  
 31 and an earlier study using a 2D hybrid code<sup>17</sup>, both of 82  
 32 which observed ion energy collapse during ITTO oscil- 83  
 33 lations. As a result, changes in the IDF over time should 84  
 34 be evident in accordance with the oscillations encoun- 85  
 35 tered. 86

36 Similar distribution shapes to those observed in B regime 87  
 37 have been reported in the literature for different operating 88  
 38 points and thrusters. For instance, the ID Hall 1 thruster 89  
 39 exhibits more distorted ion distributions functions towards high 90  
 40 energies for discharge voltages between 120 and 180 V<sup>14</sup>. The 91  
 41 ID Hall 1 thruster features a unique geometry and magnetic 92  
 42 topology, with two magnetic barriers: one being the main 93  
 43 magnetic barrier located in the channel, and the other placed 94  
 44 facing the anode. The authors found that the shape of the av- 95  
 45 eraged IDF was caused by a time-dependent change in the po- 96  
 46 tential allocation within the magnetic barriers. This was deter- 97  
 47 mined by monitoring the IDFs over time and using HALLIS 98  
 48 simulations. However, the magnetic topology of our thruster 99  
 49 is more conventional and does not have a double magnetic 100  
 50 barrier suggesting that there is another explanation to our ob- 101  
 51 servations. 102  
 103  
 104

### C. Temporal ion distribution function

After following the data collection and processing proto-  
 cols outlined in section III, the temporal evolution of the IDFs  
 for several discharge voltages (150, 240, 270, and 340 V) was  
 reconstructed.

For each discharge voltage, the figure 14 presents from  
 left to right:

- A 2D map of the ion current collected by the RPA over  
 a period corresponding to one BM oscillation, plotted  
 as a function of time (y-axis) and the energy of the ions  
 (x-axis), corrected for the cathode potential but uncor-  
 rected for the time of flight (i.e., in the RPA reference  
 frame)
- In the middle, the figure is composed of three elements:
  - A 2D map of the IDF as a function of time (y-  
 axis), calculated at the output plane of the thruster,  
 and the energy of the ions (x-axis).
  - A 1D graph on the left, which shares the same  
 time axis as the central figure, allowing us to ob-  
 serve the evolution of the average discharge cur-  
 rent and the average capacitive signal.
  - The lower 1D graph that shares the same energy  
 axis as the 2D map of  $IDF(t, E)$  and shows the  
 average IDF, calculated using  $\langle IDF(t, E) \rangle_t$ .
- Finally, the rightmost figure shows several instanta-  
 neous IDFs at fixed times. Each colour corresponds to  
 a specific instant, with the temporal positions indicated  
 by dotted lines in the central figures.

In the oscillation regime A, for  $U_d = 150$  V (figure 14 (a)),  
 as previously observed in figure 13, when examining the po-  
 sition of the most probable energy over time, we observe the  
 same significant withdrawal of around 40 eV from that im-  
 posed by the discharge voltage. Regardless of the time, the  
 distributions remain relatively symmetrical, except between  
 $-66$  and  $-22$   $\mu$ s. During this period, the resolution of the  
 IDF is more approximate, and the IDFs are noisier, despite a  
 slight decrease in the average energy of the ions of around 10  
 eV. Upon investigating the ion current for similar behaviour,  
 we observe a clear decrease in the maximum energy of the  
 ions collected between  $-32$  and  $12$   $\mu$ s. It should be noted that  
 the IDFs were reconstructed at a plane 44 cm upstream of the  
 RPA, assumed to be the thruster exit plane (the plane from  
 which the ions have completed their acceleration and have a  
 fixed velocity). Thus, since the most probable energy accord-  
 ing to the IDF during this period is around 100 eV, the time  
 of flight of the ions between the RPA and this plane should be  
 approximately  $36 \pm 3$   $\mu$ s. Taking into account an additional  
 uncertainty of a few microseconds due to approximations in  
 the definition of the region of interest, we arrive at the 44  $\mu$ s  
 difference observed, which is therefore entirely due to the time  
 of flight of the ions between the end-of-acceleration plane and  
 the RPA collector.

It should also be noted that during this period, the ion cur-

This is the author's peer reviewed, accepted manuscript. However, the online version of record will be different from this version once it has been copyedited and typeset.

PLEASE CITE THIS ARTICLE AS DOI: 10.1063/1.50235762

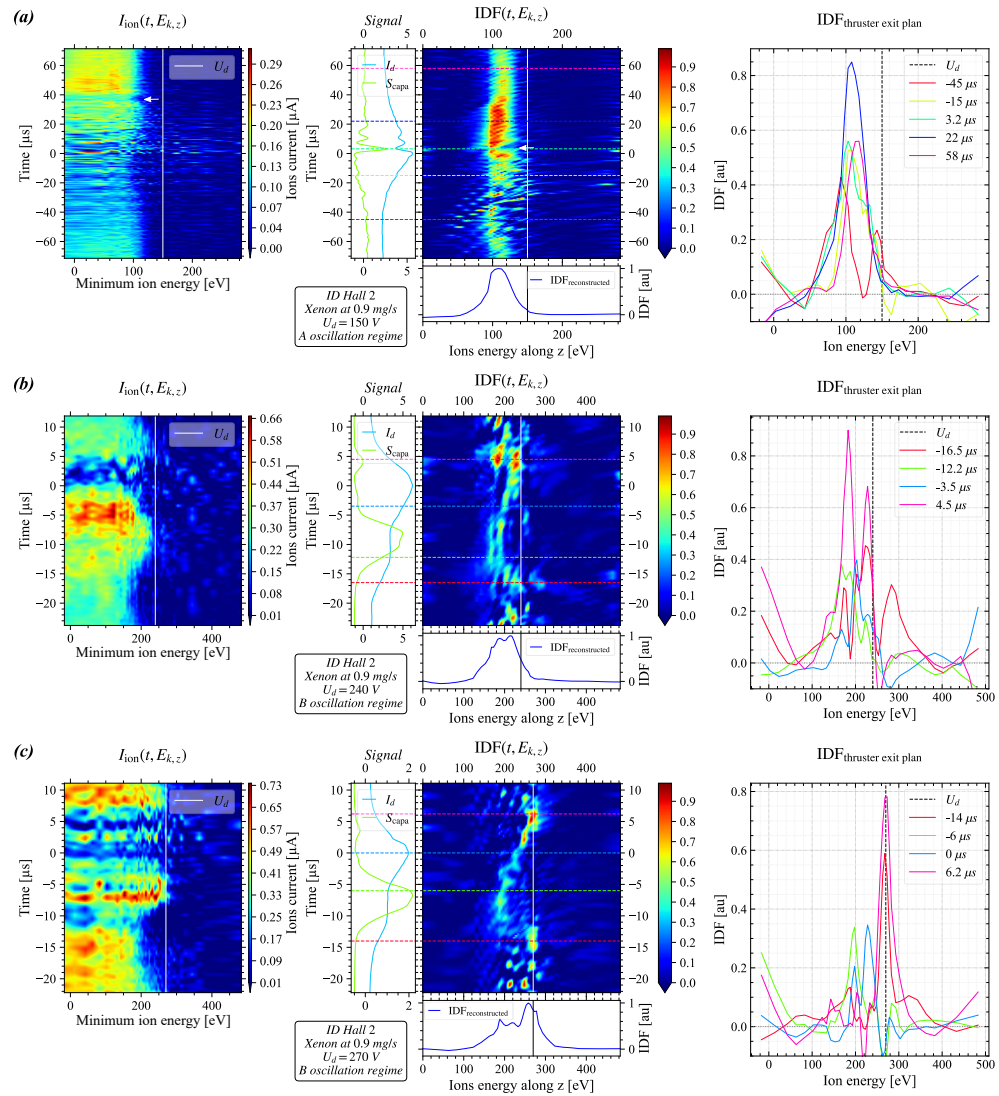


FIG. 14. From left to right: The first figure shows the 2D map of the ion current collected by the RPA over a period corresponding to a BM oscillation. The second figure presents the 2D map of the IDF as a function of time (calculated in the thruster output plane) versus ion energy (x-axis). The 1D graph on the left allows for the observation of the average discharge current and the average capacitive signal over a BM oscillation. The integrated IDF, calculated by averaging  $\langle IDF(t, E) \rangle_t$ , is plotted in the 1D graph at the bottom. Finally, on the right, the last figure displays instantaneous IDFs at fixed times. (For a mass flow rate of 0.9 mg/s and discharge voltages of 150V (a), 240 V (b), 270 V (c), and 340 V (d)).

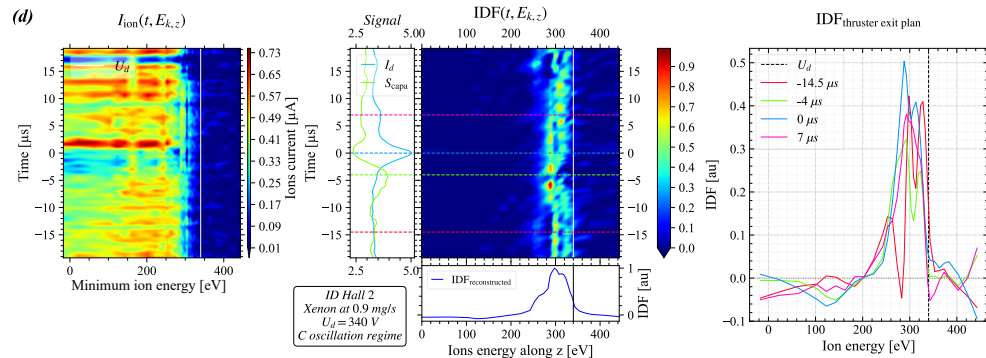


FIG. 14. From left to right: The first figure shows the 2D map of the ion current collected by the RPA over a period corresponding to a BM oscillation. The second figure presents the 2D map of the IDF as a function of time (calculated in the thruster output plane) versus ion energy (x-axis). The 1D graph on the left allows for the observation of the average discharge current and the average capacitive signal over a BM oscillation. The integrated IDF, calculated by averaging  $\langle IDF(t, E) \rangle_t$ , is plotted in the 1D graph at the bottom. Finally, on the right, the last figure displays instantaneous IDFs at fixed times. (For a mass flow rate of 0.9 mg/s and discharge voltages of 150V (a), 240 V (b), 270 V (c), and 340 V (d)).

rent collected is low ( $< 0.13 \mu A$ ), which degrades the signal-  
to-noise ratio, explaining the multiple artefacts visible in the  
distribution function, such as the "islets" with energies less  
than 90 eV or greater than 120 eV (for example, the IDF at  $-4.5$   
 $\mu s$  has two peaks, the second peak may be an artefact caused  
by the noise generated by the discharge irregularity). As time  
progresses, we also observe a brief decrease in the energy of  
the ions collected at around  $36 \mu s$  on the ion current map. The  
same decrease appears around  $1.4 \mu s$  on the IDF map. Inter-  
estingly, this brief drop in ion energy of about 15 eV occurs  
exactly when a capacitive signal pulse is recorded, attributed  
to an ITTO oscillation. For the other capacitive signal pulses  
with much lower amplitude, no modification of the ion energy  
is detected, likely due to the discharge irregularity affecting  
the averaging process.

Figures 14 (b) and (c) display the IDFs associated with  
discharge voltages of 240 V and 270 V, which correspond to  
oscillation regime B.

Let's first examine the case of  $U_d = 240$  V. As previously  
observed in figure 13, the reconstructed IDF begins to show  
significant distortion, with a considerable proportion of faster  
ions, leading to an asymmetric distribution. Initially, we ob-  
serve a variation in ion energy and the shape of the IDF on  
the same time scale as the BM oscillation. Additionally, the  
variations in  $I_d$  appear to be linked to the mean ion energy.  
Specifically, between  $-20$  and  $-13 \mu s$ ,  $I_d$  first increases while  
the ion energy collapses from approximately 220 eV to 180  
eV. Then, between  $-13$  and  $-5 \mu s$ ,  $I_d$  stabilises at a plateau,  
and the ion energy stabilises at an average of around 180 eV,  
with two distinct peaks at 170 eV and 190 eV, whose am-  
plitudes vary in opposite directions. This pattern likely does  
not reflect the true evolution of the IDFs but is probably an  
artefact caused by the reconstruction protocol applied to the

irregular discharge. During this plateau phase of  $I_d$ , a capaci-  
tive signal peak is detected, indicating a reorganisation of the  
electrical potential within the plasma. This peak is followed  
by a resumption of the increase in  $I_d$ , which is also accom-  
panied by an increase in the energy of the extracted ions, rising  
from 190 eV to 225 eV. At the beginning of the decreasing  
phase of  $I_d$ , between 0 and  $4 \mu s$ , the ion energy appears to  
remain around 225~230 eV. After  $4 \mu s$ , the situation becomes  
less clear, with the appearance of two peaks on the distribu-  
tion functions. This is illustrated by the instantaneous IDF at  
 $4.5 \mu s$ , shown by the pink curve. Unlike the evolution of the  
time-averaged IDF before  $4 \mu s$ , which is reproducible across  
multiple measurement sets, these two peaks after  $4 \mu s$  are not  
always observed.

When  $U_d$  is increased up to 270 V, we remain in regime  
B, and the results are shown in figure 14 (c). In this case,  
the temporal evolution of the IDFs is essentially the same as  
for  $U_d = 240$  V. The IDFs are still strongly distorted, with the  
maximum probability centred at high energies, and the distri-  
bution tail extends beyond the imposed discharge energy. The  
main difference is the increased gap between the minimum  
energy (185 eV at  $-8 \mu s$ ) and the maximum energy (270 eV  
at  $-14$  and  $6.2 \mu s$ ).

Finally, at  $U_d = 340$  V, when we enter regime C, we ob-  
serve quasi-symmetrical distributions, which are consistent  
with the previous integrated IDF observations (as shown in the  
C regime in figure 13). Upon examining the TIDF or the in-  
stantaneous IDF, we notice the presence of two peaks, located  
around 295 eV and 315 eV. Initially, one might assume these  
are artefacts of the measurements, caused by the irregularity  
of the discharge oscillations. This is plausible, as the irregu-  
larity becomes more pronounced as we enter the C oscillation  
regime. Moreover, above  $U_d = 340$  V, the discharge behaviour

1 becomes too irregular to be reliably reconstructed using this 57  
 2 temporal IDF method. On the map of the temporal evolution 58  
 3 of the collected ion current as a function of energy, we can see 59  
 4 that the time series corresponding to energies of 290 eV and  
 5 300 eV deviate from the others. This suggests that the general  
 6 behaviour of the discharge might have changed slightly during 60  
 7 the measurement, and the derivatives calculated at these points  
 8 may not be entirely reliable. We can note that when the average 61  
 9 capacitive signal peak is detected on our antenna, between  
 10  $-10$  and  $1 \mu\text{s}$ , the energy of the ions experiences a temporary 62  
 11 decrease, dropping from an average value of  $300\text{--}310$  eV to 63  
 12 290 eV. This observation is consistent with the simultaneous 64  
 13 observation of the capacitive pulse and the ion energy drop of 65  
 14 15 eV in regime A (figure 14 (a)). 66

15 In cases where the BM is clearly visible, we can compare 67  
 16 our results with those from a recent study by Thomas et 68  
 17 al.<sup>30</sup>, where ion distribution functions were resolved tempo- 69  
 18 rally using a different technique, Shadow Manifold Interpol- 70  
 19 ation (SMI). The shapes of the discharge currents are similar 71  
 20 between the two studies, corresponding to the oscillations ob- 72  
 21 served in our B regime. The observations regarding the shape 73  
 22 and temporal evolution of the IDFs appear to align, with an os- 74  
 23 cillation in the most probable ion energy at the BM frequency, 75  
 24 exhibiting a large amplitude exceeding 50 eV. 76

25 The key observation is that in regime B, during a single 77  
 26 BM oscillation cycle, the ion energy decreases rapidly as the 78  
 27 discharge current initially increases. When the current reaches 79  
 28 a plateau, the average ion energy remains relatively low and 80  
 29 constant. The end of this plateau coincides with a capacitive 81  
 30 signal pulse, indicating a reorganisation of the electric field 82  
 31 within the plasma. Following this, both the discharge current 83  
 32 and extracted ion energy rise again. After  $I_d$  reaches its max- 84  
 33 imum, when all gas atoms are ionised,  $I_d$  decreases rapidly. 85  
 34 However, the ion energy remains steady, at least at the be- 86  
 35 ginning of the decreasing phase, before the IDF loses reli- 87  
 36 ability due to weak and/or irregular ion current. In this con- 88  
 37 text, the capacitive pulse represents the variation in the electric 89  
 38 field, likely responsible for the ion acceleration, suggesting 90  
 39 the presence of ITTOs, even though no clear traces of them 91  
 40 are visible in the IDFs. The irregularity of the ITTO oscilla- 92  
 41 tions (as seen in figure 12) has likely led to their averaging 93  
 42 out. 94

43 Currently, we can assume that during a BM oscillation, the 95  
 44 ionization and acceleration zones move independently, which 96  
 45 alters the total electric field experienced by an ion at a given 97  
 46 location and time. Previous studies have demonstrated strong 98  
 47 correlations between the ionization and acceleration processes 99  
 48 in Hall thrusters<sup>43</sup>, with oscillations in the mean ion velocity 100  
 49 and the accelerating electric field at the breathing mode fre- 101  
 50 quency. While the final velocity of the ions is only weakly 102  
 51 dependent on the frequency of the BM oscillations, it is more 103  
 52 influenced by the position of the ionization region and the be- 104  
 53 haviour of the ions within it, particularly the backscattering 105  
 54 of ions towards the anode<sup>44</sup>. Furthermore, research has high- 106  
 55 lighted the significant role of neutral density and temperature 107  
 56 in determining the position of the ion acceleration region<sup>45</sup>. 108

Finally, several studies have demonstrated the overlap be-  
 tween the ionization and acceleration regions, combining ex-  
 perimental measurements with numerical simulations<sup>46–48</sup>.

A significant limitation of our diagnostic method is the  
 irregularity of the oscillations, which necessitates signal aver-  
 aging during data acquisition. This averaging distorts the ob-  
 served signal shapes, such as the presence of only one rapid  
 oscillation superimposed on the BM in the  $U_d = 270$  V dis-  
 charge current in figure 14, compared to the 2–3 oscillations  
 seen in figure 12. Similarly, the ion response is averaged,  
 making it appear as though there is a single continuous varia-  
 tion in the average energy of the ions. However, simulations  
 with visible ITTO on the BM show as many IDF energy fluc-  
 tuations as there are oscillations in the BM<sup>17</sup>.

To verify whether our reconstruction algorithm can re-  
 solve IDFs at frequencies in the hundreds of kHz range, it was  
 tested on the same time series from simulations presented in<sup>17</sup>.  
 Each visible BM in the collected ion currents was averaged  
 to simulate current acquisition by the RPA and oscilloscope.  
 The results obtained with our algorithm were consistent with  
 those derived from directly counting particles in the model,  
 confirming that ion distributions could be resolved with the  
 desired time resolution, even with slight discharge variability.  
 Thus, simulations suggest that ITTO oscillations in discharge  
 currents would manifest in ion energy distribution functions  
 as variations in ion energy at ITTO frequencies. However,  
 these variations were not observed in our data due to the nec-  
 essary averaging of discharge oscillations to obtain the most  
 reproducible current shape. Since ITTO oscillations are more  
 random than BM oscillations, they are effectively lost during  
 the averaging process.

## V. CONCLUSION

In this study, a technique inspired by Langmuir probe  
 time-resolved measurements was adapted for use with RPA  
 ion current measurements to reconstruct ion distribution func-  
 tions (IDFs) over time, on the scale of ITTO and BM oscilla-  
 tions. By applying this algorithm to ion currents collected  
 in each oscillation regime, we were able to explain the dif-  
 ferent shapes of integrated classical IDFs in these regimes.  
 However, the irregularity of the temporal discharge prevented  
 IDF resolution on the ITTO scale. Despite this, when the dis-  
 charge was sufficiently periodic, a modulation of the energy  
 acquired by the ions at the BM oscillation frequency was ob-  
 served, suggesting a possible uncoordinated displacement of  
 the ionization and acceleration zones. The accelerating elec-  
 tric field seen by the ions varied depending on their creation  
 time and location, with the overlap between these zones evol-  
 ving in response to BM instability.

To experimentally resolve IDFs at ITTO frequencies, it is  
 necessary to eliminate the averaging operation. One poten-  
 tial approach is to identify similar oscillation patterns in each  
 time series, which could be associated with potential RPA fil-  
 tering over a large time period. By assuming that similar ef-

This is the author's peer reviewed, accepted manuscript. However, the online version of record will be different from this version once it has been copyedited and typeset.

PLEASE CITE THIS ARTICLE AS DOI: 10.1063/5.0235762

fects produce similar consequences for ion movement at ITTO frequencies, IDFs could be reconstructed for an oscillation topology that includes both BM and ITTOs.

**AUTHOR CONTRIBUTION**

**DATA AVAILABILITY**

The data that support the findings of this study are available from the corresponding author upon reasonable request.

**NOMENCLATURE**

**Acronyms**

BM Breathing Mode  
 FFT Fast Fourier Transform  
 HT Hall Thruster  
 IDF Ion Distribution Function  
 ITTO Ions Transit Time Oscillation  
 TIDF Temporal Ion Distribution Function  
 RPA Retarding Potential Analyser

**Roman & Greek Symbols**

B Magnetic field  
 E Electric field  
  
 $e$  Elementary electric charge  
 $f(v)$  Ion velocity distribution function  
 $I_d$  Discharge current  
 $I_{e,i}$  Electron current balancing the extracted ion current  
 $I_{e,c}$  Electron current crossing the magnetic barrier  
 $I_{RPA}$  Ions current collected by the RPA  
 $m_{Xe}$  Mass of a xenon atom  
 $t$  Time  
 $U_d$  Discharge voltage  
 $S_{capa}$  Capacitive signal  
 $v$  Ion velocity  
 $V_{cg}$  Cathode potential referred to the ground  
  
 $\phi_{RPA}$  Potential of the RPA's ion filtering barrier

[T]  
 [V/m]  
  
 [C]  
 [//]  
 [A]  
 [A]  
  
 [A]  
 [kg]  
 [s]  
 [V]  
 [V]  
 [m/s]  
 [V]  
  
 [V]

**ACKNOWLEDGMENTS**

Q.D.D. has benefited from a Ph.D. funding from the French Ministry of Research. This work was supported by the CNES agency (Grant No R-S23/PF-0005-162-01). This work has been carried out within the framework of the EUROfusion Consortium, funded by the European Union via the Euratom Research and Training Programme (Grant Agreement No 101052200—EUROfusion). Views and opinions expressed are however those of the author(s) only and do not necessarily reflect those of the European Union or the European Commission. Neither the European Union nor the European Commission can be held responsible for them.

**AUTHOR DECLARATION**

**Conflict of Interest:** The authors have no conflicts to disclose.

**REFERENCES**

<sup>1</sup>A. I. Morozov, "The conceptual development of stationary plasma thrusters," *Plasma Physics Reports* **29**, 235–250 (2003).  
<sup>2</sup>D. Lev, R. M. Myers, K. M. Lemmer, J. Kolbeck, H. Koizumi, and K. Polzin, "The technological and commercial expansion of electric propulsion," *Acta Astronautica* **159**, 213–227 (2019).  
<sup>3</sup>S. Mazouffre, "Electric propulsion for satellites and spacecraft: Established technologies and novel approaches," *Plasma Sources Science and Technology* **25**, 033002 (2016).  
<sup>4</sup>D. Krejci and P. Lozano, "Space Propulsion Technology for Small Spacecraft," *Proceedings of the IEEE* **106**, 362–378 (2018).  
<sup>5</sup>E. Y. Choueiri, "Plasma oscillations in Hall thrusters," *Physics of Plasmas* **8**, 1411 (2001).  
<sup>6</sup>V. Mazières, F. Gaboriau, A. Guglielmi, V. Laquerbe, R. Pascaud, and O. Pascal, "Broadband (kHz–GHz) characterization of instabilities in Hall thruster inside a metallic vacuum chamber," *Physics of Plasmas* **29**, 072107 (2022).  
<sup>7</sup>S. Tsikata, A. Héron, and C. Honoré, "Hall thruster microturbulence under conditions of modified electron wall emission," *Physics of Plasmas* **24**, 053519 (2017).  
<sup>8</sup>Yamamoto, Kuwabara, Cho, Kosuga, and D. Pradalier, "Observation of Plasma Turbulence in a Hall Thruster Using Microwave Interferometry," *Journal of Propulsion and Power* (2023), 10.2514/1.B38711.  
<sup>9</sup>E. Chesta, C. Lam, N. Meezan, D. Schmidt, and M. Cappelli, "A characterization of plasma fluctuations within a Hall discharge," *IEEE Transactions on Plasma Science* **29**, 582–591 (Aug/2001).  
<sup>10</sup>J. Kurzyrna, S. Mazouffre, A. Lazurenko, L. Albarède, G. Bonhomme, K. Makowski, M. Dudeck, and Z. Peradzyński, "Spectral analysis of Hall-effect thruster plasma oscillations based on the empirical mode decomposition," *Physics of Plasmas* **12**, 123506 (2005).  
<sup>11</sup>L.-Q. Wei, L. Han, D.-R. Yu, and N. Guo, "Low-frequency oscillations in Hall thrusters," *Chinese Physics B* **24**, 055201 (2015).  
<sup>12</sup>K. Hara, S. Keller, and Y. Raites, "Measurements and theory of driven breathing oscillations in a Hall effect thruster," in *52nd AIAA/SAE/ASEE Joint Propulsion Conference* (American Institute of Aeronautics and Astronautics, Salt Lake City, UT, USA, 2016).  
<sup>13</sup>A. Guglielmi, A. Martín Ortega, F. Gaboriau, and J.-P. Boeuf, "Influence of double-stage operation on breathing oscillations and rotating spokes in the ID-HALL thruster," in *36th International Electric Propulsion Conference*, Vol. IEPC-2019-632 (Vienne, Autriche, 2019).  
<sup>14</sup>A. Martín Ortega, A. Guglielmi, F. Gaboriau, C. Boniface, and J. P. Boeuf, "Experimental characterization of ID-Hall, a double stage Hall thruster with an inductive ionization stage," *Physics of Plasmas* **27**, 023518 (2020).  
<sup>15</sup>V. Giannetti, M. M. Saravia, and T. Andreussi, "Measurement of the breathing mode oscillations in Hall thruster plasmas with a fast-diving triple Langmuir probe," *Physics of Plasmas* **27**, 123502 (2020).  
<sup>16</sup>M. Baird, T. Kerber, R. McGee-Sinclair, and K. Lemmer, "Plume Divergence and Discharge Oscillations of an Accessible Low-Power Hall Effect Thruster," *Applied Sciences* **11**, 1973 (2021).  
<sup>17</sup>J. Bareilles, G. J. M. Hagelaar, L. Garrigues, C. Boniface, J. P. Boeuf, and N. Gascon, "Critical assessment of a two-dimensional hybrid Hall thruster model: Comparisons with experiments," *Physics of Plasmas* **11**, 3035–3046 (2004).  
<sup>18</sup>M. F. Konopliv, R. E. Wirz, and L. K. Johnson, "Ion-Neutral Population and Electron Temperature Phasing in the Hall Thruster Breathing Mode," in *38th International Electric Propulsion Conference*, Vol. IEPC-2024-487 (Toulouse, France, 2024).

This is the author's peer reviewed, accepted manuscript. However, the online version of record will be different from this version once it has been copyedited and typeset.

PLEASE CITE THIS ARTICLE AS DOI: 10.1063/5.0235762

- 19 J. P. Boeuf and L. Garrigues, "Low frequency oscillations in a stationary plasma thruster," *Journal of Applied Physics* **84**, 3541–3554 (1998).
- 20 T. Lafleur, P. Chabert, and A. Bourdon, "The origin of the breathing mode in Hall thrusters and its stabilization," *Journal of Applied Physics* **130**, 053305 (2021).
- 21 O. Chapurin, A. Smolyakov, G. Hagelaar, J.-P. Boeuf, and Y. Raitses, "Fluid and hybrid simulations of the ionization instabilities in Hall thruster," *Journal of Applied Physics* **132**, 053301 (2022).
- 22 J. Vaudolon and S. Mazouffre, "Observation of high-frequency ion instabilities in a cross-field plasma," *Plasma Sources Science and Technology* **24**, 032003 (2015).
- 23 J. Vaudolon, *Electric Field Determination and Magnetic Topology Optimization in Hall Thruster*, Ph.D. thesis, ICARE - Institut de Combustion, Aéronautique, Réactivité et Environnement, Orléans (2015).
- 24 G. J. M. Hagelaar, J. Bareilles, L. Garrigues, and J. P. Boeuf, "Two-dimensional model of a stationary plasma thruster," *Journal of Applied Physics* **91**, 5592–5598 (2002).
- 25 F. Petronio, T. Charoy, A. Alvarez Laguna, A. Bourdon, and P. Chabert, "Two-dimensional effects on electrostatic instabilities in Hall thrusters. II. Comparison of particle-in-cell simulation results with linear theory dispersion relations," *Physics of Plasmas* **30**, 012104 (2023).
- 26 T. Gibert, L. Balika, F. Diop, and A. Bouchoule, "Doubly-Charged Xe Ions Evidenced by Time Resolved RPA Measurement in the Far Field Plume of a Low-Power HET," *Contributions to Plasma Physics* **55**, 529–537 (2015).
- 27 M. Baird, T. Kerber, K. Lemmer, and W. Huang, "Hall Thruster Plume Measurements of Time Resolved Ion Energy," in *36th International Electric Propulsion Conference*, Vol. IEPC-2019-516 (University of Vienna, Austria, 2019).
- 28 M. Baird, R. McGee-Sinclair, K. Lemmer, and W. Huang, "Time-resolved ion energy measurements using a retarding potential analyzer," *Review of Scientific Instruments* **92**, 073306 (2021).
- 29 S. Thompson, Z. Robertson, C. C. Farnell, and S. C. Farnell, "Time-Resolved Ion Measurement in the Beam Plasma of a Hall Thruster," in *38th International Electric Propulsion Conference*, Vol. IEPC-2024-818 (Toulouse, France, 2024).
- 30 A. Thomas, L. Alvesteffer, and K. Lemmer, "Time-Resolved Ion Energy Measurements of a 200-W Hall Effect Thruster with a High-Speed Retarding Potential Analyzer," in *38th International Electric Propulsion Conference* (Toulouse, France, 2024).
- 31 A. Lucca Fabris, C. V. Young, and M. A. Cappelli, "Time-resolved laser-induced fluorescence measurement of ion and neutral dynamics in a Hall thruster during ionization oscillations," *Journal of Applied Physics* **118**, 233301 (2015).
- 32 V. H. Chaplin, R. B. Lobbia, A. Lopez Ortega, I. G. Mikellides, R. R. Hofer, J. E. Polk, and A. J. Friss, "Time-resolved ion velocity measurements in a high-power Hall thruster using laser-induced fluorescence with transfer function averaging," *Applied Physics Letters* **116**, 234107 (2020).
- 33 A. Thomas and K. Lemmer, "Time-resolved ion energy measurements using a retarding potential analyzer for electric propulsion applications," *Review of Scientific Instruments* **95**, 023505 (2024).
- 34 I. Romadanov, Y. Raitses, A. Diallo, I. D. Kaganovich, K. Hara, and A. Smolyakov, "Time-resolved measurements of modulated breathing oscillations in cylindrical Hall Thruster," in *35th International Electric Propulsion Conference*, Vol. IEPC-2017-267 (Georgia Institute of Technology • Atlanta, Georgia • USA, 2017).
- 35 D. Eckhardt, J. Koo, R. Martin, M. Holmes, and K. Hara, "Spatiotemporal data fusion and manifold reconstruction in Hall thrusters," *Plasma Sources Science and Technology* **28**, 045005 (2019).
- 36 A. Loyan, F. Darnon, L. Albaredo, V. Lago, P. Lasgorceix, and M. Dudeck, "Correlation Between Hollow Cathode Operating Conditions and Hall Thruster (SPT100-ML) Performance Characteristics," in *38th AIAA/ASME/SAE/ASEE Joint Propulsion Conference & Exhibit* (American Institute of Aeronautics and Astronautics, Indianapolis, Indiana, 2002).
- 37 Q. Delavrière-Delion, F. Gaboriau, G. Fubiani, and L. Garrigues, "Experimental observation of low-frequency interactions at different scales and evidence of transit time oscillations in a Hall thruster: Spectral analysis," *Physics of Plasmas* **31**, 072110 (2024).
- 38 C. Philippe Kadlec, *Caractérisations spatio-temporelles de jets ioniques : développement des diagnostics et application à la propulsion ionique*, Ph.D. thesis, GREMI, Orléans (1998).
- 39 H. Andrei, V. Covlea, V. V. Covlea, and E. Barna, "The smoothing and the digital processing of Langmuir probe characteristic," *Romanian Reports in Physics* **55**, 51–56 (2003).
- 40 A. Caldarelli, F. Filleul, R. W. Boswell, C. Charles, N. J. Rattenbury, and J. E. Cater, "Data processing techniques for ion and electron-energy distribution functions," *Physics of Plasmas* **30**, 040501 (2023).
- 41 J. F. Caneses and B. Blackwell, "RF compensation of double Langmuir probes: Modelling and experiment," *Plasma Sources Science and Technology* **24**, 035024 (2015).
- 42 L. Nicolle, P. Sarrailh, L. Garrigues, S. Hess, and M. Villemant, "Modelling of a retarding potential analyzer and comparison with Express-A in-flight measurements," *Frontiers in Physics* **10** (2022), 10.3389/fphy.2022.862945.
- 43 S. Mazouffre and G. Bourgeois, "Spatio-temporal characteristics of ion velocity in a Hall thruster discharge," *Plasma Sources Science and Technology* **19**, 065018 (2010).
- 44 O. Chapurin, A. I. Smolyakov, G. Hagelaar, and Y. Raitses, "On the mechanism of ionization oscillations in Hall thrusters," *Journal of Applied Physics* **129**, 233307 (2021).
- 45 S. E. Cusson, E. T. Dale, B. A. Jorns, and A. D. Gallimore, "Acceleration region dynamics in a magnetically shielded Hall thruster," *Physics of Plasmas* **26**, 023506 (2019).
- 46 G. Doh, J. Park, D. Lee, H. Kim, and W. Choe, "Determination of the ionization region in Hall thruster plasmas with low perturbation," *Journal of Applied Physics* **130**, 193301 (2021).
- 47 L. Garrigues, S. Mazouffre, and G. Bourgeois, "Computed versus measured ion velocity distribution functions in a Hall effect thruster," *Journal of Applied Physics* **111**, 113301 (2012).
- 48 W. Hargus and M. Nakles, "Ion Velocity Measurements Within the Acceleration Channel of a Low-Power Hall Thruster," in *30th International Electric Propulsion Conference*, Vol. IEPC-2007-172 (Florence, Italia, 2007).